

Resonant Tunneling in Graphene Pseudomagnetic Quantum Dots

Zenan Qi,^{†,||} D. A. Bahamon,^{‡,||} Vitor M. Pereira,^{*,‡} Harold S. Park,[†] D. K. Campbell,[§]
and A. H. Castro Neto^{‡,§}

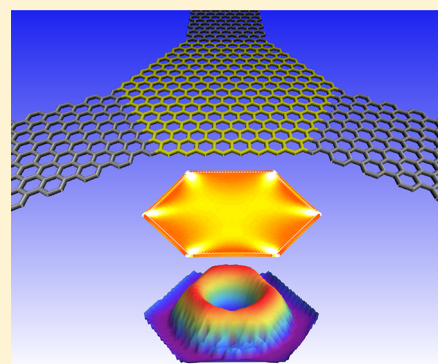
[†]Department of Mechanical Engineering, Boston University, Boston, Massachusetts 02215, United States

[‡]Graphene Research Centre and Department of Physics, National University of Singapore, 2 Science Drive 3, Singapore 117542

[§]Department of Physics, Boston University, Boston, Massachusetts 02215, United States

Supporting Information

ABSTRACT: Realistic relaxed configurations of triaxially strained graphene quantum dots are obtained from unbiased atomistic mechanical simulations. The local electronic structure and quantum transport characteristics of γ -junctions based on such dots are studied, revealing that the quasi-uniform pseudomagnetic field induced by strain restricts transport to Landau level- and edge state-assisted resonant tunneling. Valley degeneracy is broken in the presence of an external field, allowing the selective filtering of the valley and chirality of the states assisting in the resonant tunneling. Asymmetric strain conditions can be explored to select the exit channel of the γ -junction.



KEYWORDS: Graphene, strain, magnetic quantum dots, quantum transport, pseudomagnetic fields, atomistic calculations

Endowed with the strongest covalent bonding in nature, graphene exhibits the largest tensional strength ever registered ($E \approx 1$ TPa) and a record range of elastic deformation for a crystal, which can be as high as 15–20%.^{1,2} Such outstanding mechanical characteristics are complemented by an unusual coupling of lattice deformations to the electronic motion, that can be captured by the concept of a pseudomagnetic field (PMF) arising as a result of nonuniform local changes in the electronic hopping amplitudes.^{3–5} Since electrons in graphene respond to these local PMFs precisely as they would to a real magnetic field, this specific strain-induced perturbation is not screened by the free electrons in the same way that the usual displacement field coupling can be. Consequently, the ability to manipulate the strain distribution in graphene opens the enticing prospect of strain-engineering its electronic and optical properties, as well as of enhancing interaction and correlation effects.^{6–11} The recent experimental confirmation that PMFs in excess of 300 T are possible with modest deformations in structures spanning only a few nanometers^{12,13} brings this prospect of strongly impacting graphene's electronic properties by strain closer to fruition.

Despite this recent experimental evidence for strong PMF-induced Landau quantization, to the best of our knowledge no measurements or calculations have been performed to assess the transport characteristics of such nanostructures. The ability to produce very large and fairly homogeneous PMFs within a few nanometers suggests the possibility of creating pseudomagnetic quantum dots, where confinement is driven by the PMF. Here we undertake a theoretical study to probe the electronic and quantum transport properties of a representative

graphene-based strained γ -junction particularly suited to the generation of quasi-uniform PMFs.⁶ We assess the quantum transport characteristics of such structures, revealing the Landau level- (LL) assisted character of the tunneling mechanism, as well as the interplay with an external field that breaks the valley degeneracy.

Calculation Methodology. In order to capture the microscopic details as realistically as possible, we employed a combined atomistic, electronic, and transport calculation procedure, which provides a set of unbiased results at all these levels. The microscopic configuration of each carbon atom is obtained by a fully relaxed molecular mechanics (MM) approach which, together with Monte Carlo approaches,¹⁴ constitutes one of the most unbiased ways to describe deformation fields in nanostructures. Knowledge of the position of each atom allows us to extract the π -band bandstructure of the relaxed lattice via a tight-binding (TB) approach, as well as to calculate the quantum transport properties across the structure via a nonequilibrium Green's function (NEGF) approach. In this way, one unveils the local electronic structure from which we can extract, for example, the local PMFs and local current distribution, without approximations, using a system with more than 6000 atoms.

The deformed configurations of an hexagonal graphene monolayer were obtained using standard MM simulations at 0

Received: March 8, 2013

Revised: May 8, 2013

Published: May 9, 2013

K with LAMMPS.¹⁵ For definiteness, we shall focus here on the system shown in Figure 1 with 6144 atoms and a side length, L

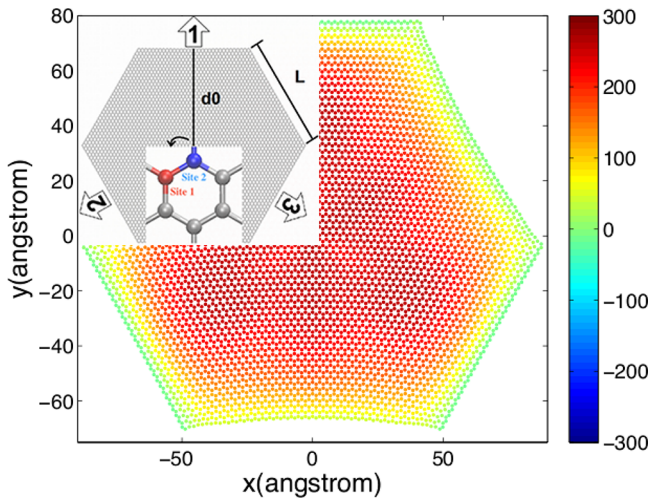


Figure 1. Real-space distribution of the PMF B_s (Tesla) under $\epsilon_{\text{eff}} = 15\%$ obtained by mapping the tight-binding-derived LDOS at each atom. Inset: diagram of the triaxial loading and contact scheme. $L \simeq 8$ nm.

$= 7.87$ nm, but we stress that the results do not show variance among specific sizes and can be straightforwardly rescaled to larger or smaller dimensions.^{16,17} The carbon interactions were modeled via the AIREBO potential¹⁸ with a cutoff at 0.68 nm, which has been shown to capture accurately the mechanical properties of carbon-based nanostructures, including bond breaking, deformation, and various elastic moduli.^{19–21} Additional details are discussed in the Supporting Information.¹⁷ The system was triaxially stretched by in-plane displacement increments of 10^{-3} nm along each of the three arms shown in Figure 1. Following each strain increment, graphene was allowed to relax according to the conjugate gradient algorithm, until relative changes in the system energy from one increment to the next were smaller than 10^{-7} . Because the strain thus generated is nonuniform, we introduce the nominal strain $\epsilon_{\text{eff}} = (d - d_0)/d_0$, where $d_0(d)$ is the distance from the center to the edge of the hexagon before (after) stretching, as illustrated in Figure 1. Nominal strains ranging from 0 to 18% are considered below.

Once the relaxed configurations were obtained at each value of strain, the atomic positions were used as the basis for

electronic structure and quantum transport calculations. Specifically, we used the relaxed atomic positions as input to the exact diagonalization of the π -band TB Hamiltonian for graphene, using the parametrization $V_{pp\pi}(l) = t_0 e^{-3.37(l/a-1)}$ to describe the dependence of this Slater-Koster parameter on the C–C distance l ($t_0 = 2.7$ eV and $a \simeq 0.142$ nm). This approximation was shown to describe with good accuracy both the threshold deformation for the Lifshitz band insulator transition at large deformations,^{22,23} and the behavior of $V_{pp\pi}(l)$ or the optical conductivity when directly compared to ab initio calculations.^{8,24} Here we do not consider electron–electron interactions.

One property that we extract from this procedure is the exact (within this TB model) local density of states (LDOS), from which we can map the local PMF distribution by fitting the resonant LDOS at each atom to the Landau level (LL) spectrum expected for graphene^{5,25}

$$E_n = \pm \hbar \omega_c \sqrt{n}, \quad \hbar^2 \omega_c^2 = 2e \hbar v_F^2 B_s, \quad \hbar v_F = \frac{3ta}{2} \quad (1)$$

An example of typical LDOS spectra is shown in Figure 2a. Equation 1 is used to obtain the local B_s distribution throughout the system by fitting the slope of E_n versus \sqrt{n} seen in the numerical LDOS at various strains, as shown in Figure 2b. Notice how the $n = 0$ LL is absent in the LDOS of one of the sublattices, similarly to data recently reported in experiments with artificial honeycomb lattices.²⁶

To complement this exact numerical calculation of B_s at each lattice point, we used another approach for comparison and control. It hinges upon the strain-induced perturbation to the continuum Dirac equation that is applicable at low energies.^{4,6,27} In this approach one uses $B_s = \partial_x A_y - \partial_y A_x$, where the fictitious vector potential for an electron (charge $-e$) is given by

$$A_x = -\frac{3t\beta}{4ev_F}(\epsilon_{xx} - \epsilon_{yy}), \quad A_y = -\frac{3t\beta}{2ev_F}(-\epsilon_{xy}) \quad (2)$$

and $\beta = -a((\partial \ln V_{pp\pi}(l))/(\partial l)) \approx 3.37$, the same used in our TB parametrization. The key here is to obtain the space-dependent strain tensor $\epsilon_{ij}(r)$. It can be obtained directly from the displacements during the MM calculation and affords an alternative method to extract $B_s(r)$ in the entire system more expeditiously. We shall refer to this as the “displacement approach” and use it to map the PMF distribution, thus assessing the range of validity of this “displacement approach +

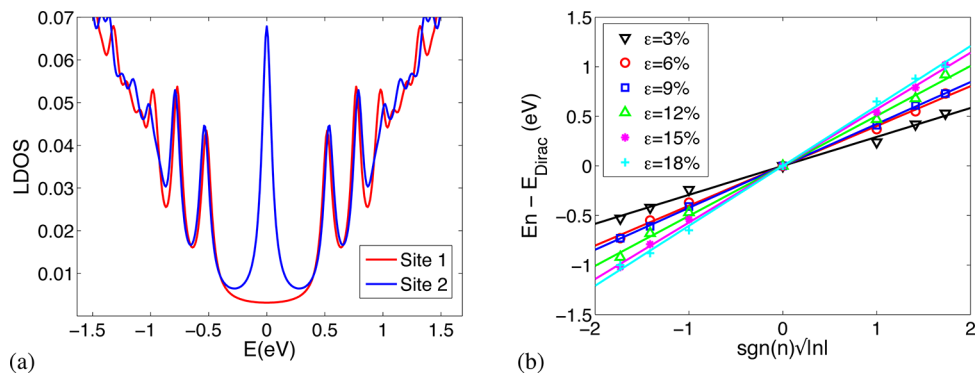


Figure 2. (a) LDOS at two representative neighboring sites (Figure 1) for $\epsilon_{\text{eff}} = 15\%$. Peak positions versus $\text{sgn}(n)(|n|)^{1/2}$, extracted from spectra such as (a), and for different ϵ_{eff} . Straight lines are fits to eq 1 from which we extract the local B_s at the site where the LDOS was sampled.

Dirac equation” in comparison with the direct TB on the deformed lattice.¹⁷

PMF Distribution. Recent experiments show in a spectacular way how strain can impact the electronic properties of graphene by confirming the existence of strain-induced LLs corresponding to fields from 300 to 600 T in graphene nanobubbles.^{12,13} Our approach of sampling the LDOS and fitting the LL resonances to eq 1, as illustrated in Figure 2, is the theoretical analog of the STM analysis done in those experiments. The real space PMF distribution for $\epsilon_{\text{eff}} = 15\%$ is shown in Figure 1 and follows the general predictions of Guinea et al.⁶ Most notably, the PMF is nearly uniform in most of the inner portion, which is a consequence of the trigonal loading conditions. This field uniformity is crucial to have well-defined LLs at nominal strains as small as 3%. To quantify the dependence of the field on the nominal strain we plot the maximum, B_s^{max} at the center of the hexagon in Figure 3,

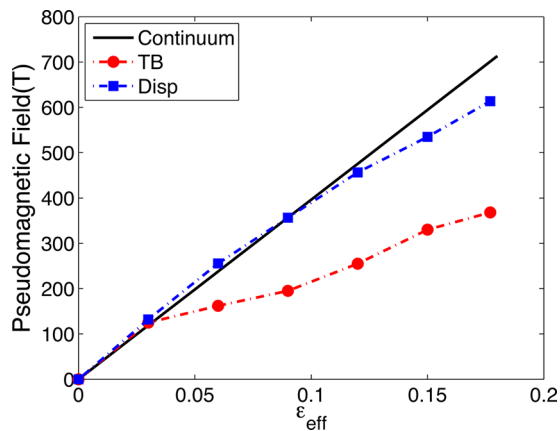


Figure 3. Dependence of B_s^{max} on ϵ_{eff} obtained by the tight-binding and displacement approaches discussed in the text.

showing that for the parameter β used here and at small ϵ_{eff} each 1% of nominal strain increases B_s^{max} by ≈ 40 T. Direct comparison of the curves generated by the two methods mentioned above shows that B_s obtained using the displacement approach begins overestimating B_s beyond $\epsilon_{\text{eff}} \sim 5\%$. This is expected insofar as eq 2 results from an expansion of $V_{\text{pp}\pi}(l)$ to linear order in ϵ_{eff} and hence is bound to overestimate the rate of change of $V_{\text{pp}\pi}$ (and thus B_s) at higher deformations. On the basis of our data at low ϵ_{eff} we extract the scaling $B_s^{\text{max}} = C\epsilon_{\text{eff}}/L$ with $C \approx 3 \times 10^4$ T nm. This relation can be used to obtain B_s for systems with any L and ϵ_{eff} . For large ϵ_{eff} the data in Figure 3 must be taken into account to correct for the overestimate. The magnetic lengths, l_B , associated with these large PMFs can easily become comparable to the system size, and thus a strong interplay between magnetic and spatial confinement is expected. In particular, the small size of the quantum dot implies that most low energy states will not be “condensed” into LLs,²⁸ and in addition resonant transport behavior can be seen in these structures as a result of tunneling assisted by the magnetically confined states in the central region. This is characterized next.

Quantum Transport. To calculate the quantum transport characteristics of the strained hexagon we coupled three unstrained semi-infinite metallic AC graphene nanoribbons to the sides of the ZZ hexagon where the load is applied (cf. inset of Figure 1), thereby creating a y -junction. There is no barrier

between the metallic contacts and the central region, and the only perturbation to the electronic motion arises from the strain-induced changes in the nearest neighbor hoppings inside the hexagon. The width of the contacts coincides with the side, L , of the hexagon. In a multicontact device the current in the p -th contact is expressed using the Landauer-Büttiker formalism as $I_p = (2e^2)/(\hbar) \sum_q [T_{qp}V_p - T_{pq}V_q]$.²⁹ With no loss of generality, a bias voltage V_1 is applied to contact 1, while contacts 2 and 3 are grounded. In this configuration $I_1 = (2e^2)/(\hbar)[T_{21} + T_{31}]V_1$, $I_2 = -(2e^2)/(\hbar)T_{21}V_1$ and $I_3 = -(2e^2)/(\hbar)T_{31}V_1$, reducing the calculations to the transmission coefficient between contact 1 and 2: T_{21} ($T_{31} = T_{21}$ under symmetric loading). The transmission coefficient is given by $T_{qp} = \text{Tr}[\Gamma_q G^r \Gamma_p G^a]$, where the Green’s functions are $G^r = [G^a]^\dagger = [E + i\eta - H - \Sigma_1 - \Sigma_2 - \Sigma_3]^{-1}$, the coupling between the contacts and the device is $\Gamma_q = i[\Sigma_q - \Sigma_q^\dagger]$, and Σ_q is the self-energy of contact q , all of them calculated numerically.³⁰

Figure 4a shows the transmission coefficient T_{21} ($=T_{31}$ under symmetric loading) as a function of the Fermi energy, E_F , for

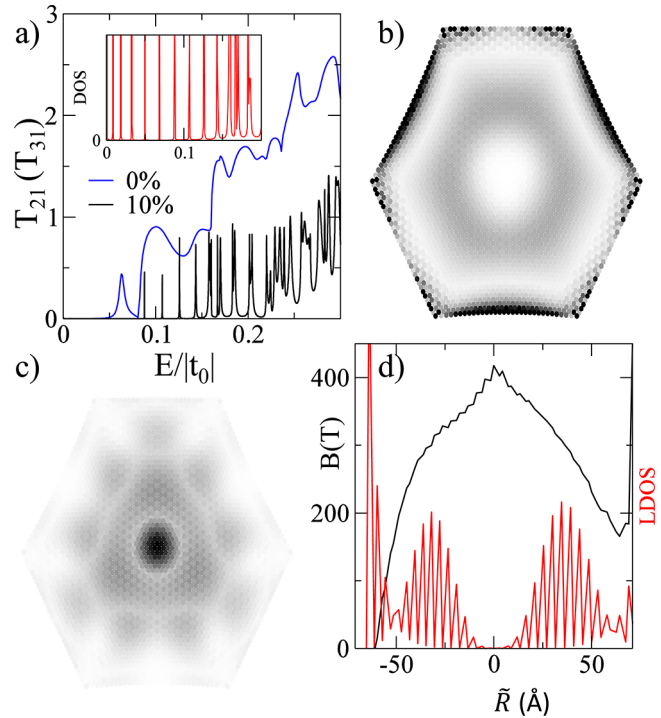


Figure 4. (a) Transmission coefficient $T_{21}(T_{31})$ versus E_F for $\epsilon_{\text{eff}} = 0$ and 10%. The inset shows a close-up of the total DOS of the strained dot in the low energy region. A LDOS map (white is zero) of selected transmission resonances for $\epsilon_{\text{eff}} = 10\%$ is shown in (b) for $E = 0.018t_0$, and (c) for $E = 0.16t_0$. (d) A transverse section of (b) along the vertical direction through the center of the hexagon, showing the profile of the LDOS and the PMF (displacement approach). \bar{R} marks the distance to the center.

the y -junction of Figure 1. The smooth (blue) curve is the transmission in the absence of strain, and the resonant trace (black) the transmission for $\epsilon_{\text{eff}} = 10\%$. The unstrained junction’s transmission is characterized by a threshold and a broad resonance around $E/t_0 \approx 0.063$, and a set of broad resonances and antiresonances on a smooth background as E increases. The resonance at the threshold marks the fundamental mode of the hexagonal cavity which, from the geometry, is estimated to appear at $E \approx \hbar v_F(\pi/\sqrt{2}L) = 0.06t_0$.

Spatial mapping of the LDOS (not shown) at this energy confirms this.

Upon stretching, the following three different regions can be identified in the curve of $T_{21}(E)$ in Figure 4a: (i) at low energies the transmission is suppressed; (ii) at intermediate energies the transmission develops a series of regularly spaced sharp resonances; and (iii) at higher energies the transmission shows unevenly spaced and rapidly oscillating peaks. To characterize these different regimes we resort to the features of the overall DOS, as well as the LDOS distribution, $N(r, E) = (-1/\pi) \text{Im}[G^r(r, r; E)]$, at representative energies. The DOS is shown in the inset of Figure 4a and, even though there are plenty of low energy states, only those above $E \approx 0.08 t_0$ have an appreciable signature in the transmission. To understand this absence of transmission we turn to Figure 4b, which plots a real-space LDOS map of a state at $E = 0.018 t_0$, representative of these low energy states that have no signature in the transmission. Apart from the nonpropagating LDOS accumulation at the ZZ edges, the significant LDOS amplitude is distributed within an annulus of radius ≈ 4 nm and width ≈ 2.5 nm. Since the LDOS does not extend to the vicinity of the contacts, revealing a small coupling between this state and the modes of the contacts, the only possibility for transmission is through tunneling. But since the spatial barrier for tunneling into this confined state is rather large (≈ 2.5 nm), the resonant peak in the transmission associated with this state has a vanishingly small amplitude and is not seen on the scale of Figure 4. A transverse cut of the LDOS in Figure 4b along the vertical direction through the hexagon center is shown in Figure 4 panel d.¹⁷ It reflects the wave function of a PMF-induced Landau edge state confined to the hexagonal quantum dot, analogous to the edge states in magnetic quantum dots.²⁸ As the energy is progressively increased, the associated states spread out, approaching the boundaries. Their coupling to the contacts increases until the tunneling-assisted conductance becomes of the order of the conductance quantum and the associated transmission resonances become visible in the black trace of Figure 4b.

The LDOS map in Figure 4c corresponds to $E = 0.16 t_0$ and typifies the behavior at higher E_F . It is clear that this state is completely different from the one in Figure 4b, as its LDOS spreads over the entire dot and is highly peaked at the center. It corresponds to a state in the $n = 1$ LL. The rapid oscillations in the transmission coefficient and DOS at that energy are also consistent with this interpretation.³¹ An additional quantitative confirmation is given as follows. If the state at $E = 0.16 t_0$ belongs to the $n = 1$ LL, its associated magnetic length will be $l_{B_s} = \sqrt{2\hbar v_F/E_{n=1}} \approx 1.9$ nm. The energy difference between Landau edge states whose energy is between $E_{n=0}$ and $E_{n=1}$ can be estimated by dividing the LL separation by the number of edge states per LL: $\Delta E \approx (E_{n=1} - E_{n=0})/l_{B_s}/2L_0 \approx 0.02 t_0$, where the factor $2L_0/l_{B_s}$ corresponds to the average number of edge states between these two Landau levels.³¹ Inspecting the inset of Figure 4a we verify that the level spacing below $E \approx 0.1 t_0$ is indeed $\sim 0.02 t_0$. Moreover, given that this quantitative estimate is consistent, we can extract the average magnetic field determining the transport behavior, which is $B_s^{\text{av}} = \hbar/e l_{B_s}^2 \approx 164$ T. This value, obtained independently and solely from the transmission characteristics, expectedly corresponds to the PMF in the region of maximum LDOS for this state, from Figure 4d and, correcting for the overestimation in the PMFs

obtained from the displacement approach in Figure 3, that would be $\approx 270/1.6 = 169$ T.

Hence, transport in the strained junction is characterized by LL-assisted resonant tunneling, analogously to a magnetic quantum dot, with the novelty that here the Landau quantization arises from the strain-induced PMF, B_s . Because of the effective magnetic barrier, electrons injected from contact 1 can tunnel with a probability $0 < T < 1$, which is enhanced when there is significant LDOS in the contact region. The maximum tunneling probability through a localized state is $T = 1$, irrespective of the number of open channels in the contacts. This implies that between the LL $n = 0$ and $n = 1$ we expect $T_{21}^{\text{max}} = 0.5$ (0.5 because there are two symmetric exit channels). However each LL with $n \neq 0$ in graphene is doubly degenerate, and hence $T_{21}^{\text{max}} = 1$, which is consistent with the calculated transmission seen in Figure 4a, where $T_{21}(E = 0.126 t_0) = 0.79$, for example.

Valley Splitting. The strain-induced PMF does not break time-reversal symmetry (TRS) in the system, which in practice means that a low energy electron around one of the zone-edge valleys feels a PMF which is exactly the opposite to the one felt by its TRS counterpart at the other inequivalent valley. This leads to the degeneracy discussed above and, in addition, to the result that the currents associated with the two valleys exactly cancel each other. This degeneracy is lifted under a real magnetic field, B_{ext} , since the total field at each valley will be different: $B_{\text{ext}} \pm B_s$. The corresponding LL splitting is given by $E_n^+ - E_n^- \approx E_n B_{\text{ext}}/B_s^{\text{av}}$. In Figure 5a, we show explicitly this

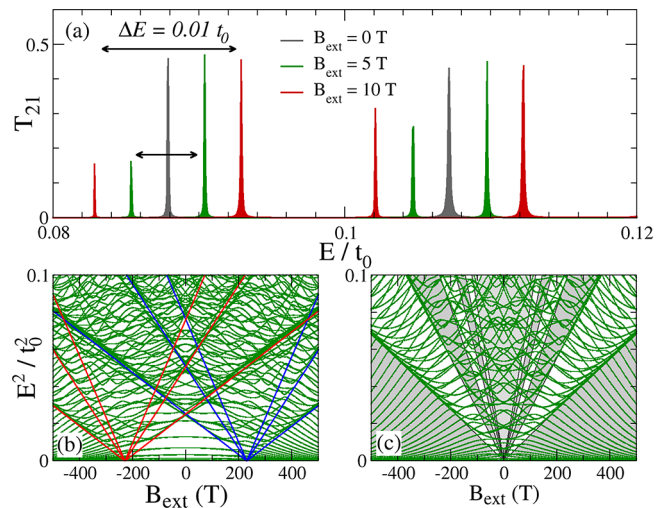


Figure 5. (a) Detail of the splitting in the T_{21} resonances under an external field B_{ext} , for $\epsilon_{\text{eff}} = 10\%$. (b) Eigenenergies of the same hexagon versus B_{ext} when disconnected from the contacts. (c) Likewise but for $\epsilon_{\text{eff}} = 0$, where LL condensation²⁸ is more clearly observed. In (b,c), straight lines mark the lowest LLs in the infinite system, and the large range of B_{ext} used in the horizontal axes is to accommodate the very large PMF induced by strain.

splitting for the edge states detached from the $n = 1$ LL. Taking the values estimated above for $B_s^{\text{av}} \approx 164$ T, and $E_{n=1} \approx 0.16 t_0$, the expected splitting under the external field is $(E^+ - E^-)/t_0 \approx 0.001 B_{\text{ext}} T^{-1}$. Direct inspection of Figure 5a shows that this is indeed quantitatively verified. A different perspective over the splitting of valley degeneracy is given in Figure 5b, which shows the spectrum of the strained hexagon disconnected from the contacts, as a function of B_{ext} . When compared with the

unstrained case in Figure 5c, one sees that the effect of the large PMF induced by strain is to split the Landau fan, which is a clear evidence of valley degeneracy breaking. Notice also that this degeneracy breaking is visibly achieved under 10 T, as shown in Figure 5a.

Another interesting consequence of breaking the valley degeneracy is that, as B_{ext} increases, the edge states in one valley will shrink to a smaller radius than in Figure 4(b), whereas the ones associated with the other will expand due to the opposite evolution of the respective magnetic lengths. Therefore, by increasing B_{ext} one can spatially “expand” the edge states of one valley [cf. Figure 4b] so that they start coupling more effectively with the leads. This is reflected in Figure 5 by the asymmetry in T_{12} of the split transmission resonances: the state which increases in energy under B_{ext} is the one whose l_B increases, thereby facilitating the resonant tunneling process, and displaying higher transmission than its counterpart associated with the other valley. Consequently, with an external field one can restrict the assisted tunneling to states from one or the other valley. The current path will then have a well-defined chirality depending on which valley is assisting the tunneling. This suggests the possibility of exploring this chiral resonant tunneling to channel the current from lead 1 selectively to lead 2 or 3.

Asymmetry, Disorder, and Lattice Orientation. The triaxial strain profile of Figure 1 was chosen in this investigation as it provides a nearly optimal PMF distribution within the nanostructure.⁶ However, the magnitude of the PMF will depend on the relative orientation of traction and crystal directions, implying that the magnitude of the confining effects, for example, is sensitive to that orientation. This is a general feature of strain induced PMFs in graphene. Likewise, nonsymmetric triaxial tension perturbs the PMF distribution as well, which has consequences for the electronic behavior. For a perspective on this, we discuss the transport behavior for different lattice orientations, as well as asymmetric tension, in the Supporting Information.¹⁷ An analysis of the consequences of edge roughness¹⁷ shows that the LL-assisted tunneling is sensitive to the amount of roughness at the boundaries, which is expected since the large PMF at the center of the hexagon forces the current to flow close to the boundary. In this sense, the experimental exploration of the LL-assisted tunneling described here is more straightforwardly observable in graphene structures synthesized via bottom-up microscopic approaches,^{32,33} or artificial graphene structures,^{26,34} where the effects of fabrication-induced disorder can be minimized. With respect to the strain symmetry, we observe that extreme deviations from symmetric traction deteriorate the LL-assisted resonant tunneling that is possible under the conditions discussed above. This arises because asymmetric strain displaces the region of strong field toward one of the boundaries. This, on the other hand, can be explored to selectively block one of the output contacts in the y-junction, allowing control over which of the two is the exit channel. A specific case is analyzed in the Supporting Information.

Conclusion. The unparalleled elastic properties of graphene and the unusual response of its electrons to deformations captured by the PMF concept imply that nanostructures deformed with the right symmetry can behave as magnetic quantum dots. Conductance at low E_F is limited to edge state-assisted resonant tunneling, and the valley degeneracy can be explicitly broken under an external field, allowing control over which valley assists in the tunneling process. Since B_s can easily

reach hundreds of Tesla in experiments,^{12,13} such small pseudomagnetic quantum dots are a viable prospect and certainly warrant further investigation.

■ ASSOCIATED CONTENT

Supporting Information

Details are provided of the MM simulations and displacement loading strategies, the dependence of conductance characteristics on the relative orientation between lattice and deformation field, the consequences of edge roughness and nonsymmetric strain fields, and the local current distribution inside the dot for the representative cases studied. This material is available free of charge via the Internet at <http://pubs.acs.org>.

■ AUTHOR INFORMATION

Corresponding Author

*E-mail: vpereira@nus.edu.sg.

Author Contributions

||Z.Q. and D.A.B. contributed equally to this work.

Notes

The authors declare no competing financial interest.

■ ACKNOWLEDGMENTS

This work was supported by the NRF-CRP award “Novel 2D materials with tailored properties: beyond graphene” (R-144-000-295-281). Z.Q. and H.S.P. acknowledge the support from NSF Grant CMMI-1036460, Banco Santander, and from the Mechanical Engineering Department of Boston University. H.S.P. further acknowledges support from a Boston University Discovery Grant.

■ REFERENCES

- (1) Lee, C.; Wei, X.; Kysar, J. W.; Hone, J. *Science* **2008**, *321*, 385–388.
- (2) Cadelano, E.; Palla, P. L.; Giordano, S.; Colombo, L. *Phys. Rev. Lett.* **2009**, *102*, 235502.
- (3) Kane, C. L.; Mele, E. J. *Phys. Rev. Lett.* **1997**, *78*, 1932.
- (4) Suzuura, H.; Ando, T. *Phys. Rev. B* **2002**, *65*, 235412.
- (5) Castro Neto, A. H.; et al. *Rev. Mod. Phys.* **2009**, *81*, 109–162.
- (6) Guinea, F.; Katsnelson, M. I.; Geim, A. K. *Nat. Phys.* **2010**, *6*, 30–33.
- (7) Pereira, V. M.; Castro Neto, A. H. *Phys. Rev. Lett.* **2009**, *103*, 046801.
- (8) Pereira, V. M.; et al. *Eur. Phys. Lett.* **2010**, *92*, 67001.
- (9) Pellegrino, F. M. D.; Angilella, G. G. N.; Pucci, R. *Phys. Rev. B* **2010**, *81*, 035411.
- (10) Abanin, D. A.; Pesin, D. A. *Phys. Rev. Lett.* **2012**, *109*, 066802.
- (11) Sharma, A.; Kotov, V. N.; Castro Neto, A. H. *Phys. Rev. B* **2013**, *87*, 155431.
- (12) Levy, N.; et al. *Science* **2010**, *329*, 544–547.
- (13) Lu, J.; Castro Neto, A. H.; Loh, K. P. *Nat. Commun.* **2012**, *3*, 823.
- (14) Los, J. H.; Katsnelson, M. I.; Yazyev, O. V.; Zakharchenko, K. V.; Fasolino, A. *Phys. Rev. B* **2009**, *80*, 121405.
- (15) Plimpton, S. J. *Comput. Phys.* **1995**, *117*, 1–19.
- (16) The lattice orientation is nevertheless important, and we chose the one in Figure 1, which maximizes the magnitude of the PMF.⁶
- (17) See also the accompanying Supporting Information.
- (18) Stuart, S. J.; Tutein, A. B.; Harrison, J. A. *J. Chem. Phys.* **2000**, *112*, 6472–6486.
- (19) Zhao, H.; Min, K.; Aluru, N. R. *Nano Lett.* **2009**, *9*, 3012–3015.
- (20) Wang, M.; et al. *Comput. Mater. Sci.* **2012**, *54*, 236–239.
- (21) Qi, Z. N.; et al. *Nanotechnology* **2010**, *21*, 7.
- (22) Pereira, V. M.; Castro Neto, A. H.; Peres, N. M. R. *Phys. Rev. B* **2009**, *80*, 045401.

- (23) Ni, Z. H.; et al. *ACS Nano* **2009**, *3*, 483.
- (24) Ribeiro, R. M.; et al. *New J. Phys.* **2009**, *11*, 115002.
- (25) McClure, J. W. *Phys. Rev.* **1956**, *104*, 666.
- (26) Gomes, K. K.; et al. *Nature* **2012**, *483*, 306–310.
- (27) Vozmediano, M. A. H.; Katsnelson, M. I.; Guinea, F. *Phys. Rep.* **2010**, *496*, 109–148.
- (28) Lent, C. S. *Phys. Rev. B* **1991**, *43*, 4179–4186.
- (29) Datta, S. *Electronic Transport in Mesoscopic Systems*; Cambridge University Press: New York, 1995.
- (30) Bahamon, D. A.; Pereira, A. L. C.; Schulz, P. A. *Phys. Rev. B* **2010**, *82*, 165438.
- (31) Sivan, U.; Imry, Y.; Hartzstein, C. *Phys. Rev. B* **1989**, *39*, 1242–1250.
- (32) Zhi, L.; Mullen, K. *J. Mater. Chem.* **2008**, *18*, 1472.
- (33) Cai, J.; et al. *Nature* **2010**, *466*, 470.
- (34) Park, C.-H.; Louie, S. G. *Nano Lett.* **2009**, *9*, 1793.